High-resolution zero-kinetic-energy pulsed field ionization photoelectron spectra of the Na(H_2O) complex

Kwanghsi Wang, David A. Rodham, and Vincent McKoy
Division of Chemistry and Chemical Engineering, California Institute of Technology, Pasadena, California 91125

Geoffrey A. Blake
Division of Geological and Planetary Sciences, California Institute of Technology, MS 150-21, Pasadena, California 91125

(Received 29 August 1997; accepted 17 December 1997)

Measured single-photon zero-kinetic-energy pulsed field ionization (ZEKE-PFI) photoelectron spectra of the sodium–water complex are presented and compared with the results of rotationally resolved *ab initio* calculations. The very nonatomiclike behavior of the photoionization of this Na(H_2O) complex is essential in accounting for several significant features in these spectra. Agreement between the calculated and measured photoelectron spectra is encouraging. Furthermore, these results suggest that combined experimental and theoretical studies of ZEKE-PFI spectra can be very useful in elucidating the molecular structure and intermolecular force fields of small clusters. © *1998 American Institute of Physics.* [S0021-9606(98)01112-X]

I. INTRODUCTION

Photoelectron spectroscopy has long been an indispensable tool in the investigation of the electronic and vibrational properties of polyatomic molecules and their ions. Furthermore, rotationally resolved photoelectron spectra can help elucidate molecular structure and provide insight into the underlying photoionization dynamics.[1] While conventional photoelectron spectroscopy achieves rotational resolution only for the lightest species such as hydrides, the recent development of zero-kinetic-energy pulsed field ionization (ZEKE-PFI) photoelectron spectroscopy is enabling dramatic advances in the experimental characterization of polyatomic cations at high spectral resolution. Indeed, the ability of ZEKE spectroscopy to give either fully or partially rotationally resolved spectra of molecular ions is well-documented.[2–4] In ZEKE-PFI spectroscopy, narrow-band laser radiation is used to prepare high-n long-lived Rydberg states lying a few cm^{-1} below each ion threshold. After a suitable delay (typically some 1–3 ms) during which kinetic electrons exit the extraction region of the ion source, a small voltage is applied to one extraction plate, creating an electric field which ionizes these high-n states and accelerates the ZEKE electrons toward a microchannel plate or other electron detector. By scanning the laser and collecting this pulsed-field electron signal, a photoionization spectrum can be obtained with resolution approaching 0.1 cm^{-1}.

Accompanying these dramatic advances in experimental techniques are equally pivotal breakthroughs in the ability to carry out robust calculations of high-resolution molecular photoelectron spectra.[3,5,6] The essential task in studies of molecular photoionization is the determination of the molecular orbitals which describe the motion of the photoelectron in the field of the molecular ion and define the photoionization matrix elements. The anisotropic potential of molecular ions leads to angular momentum coupling in the photoelectron wave functions which, in turn, can exert significant influence on ion rotational distributions. Numerical techniques for obtaining these photoelectron wave functions have been developed[7] and used to study rotationally resolved photoelectron spectra in a wide range of molecules. Such efforts highlight the rich underlying dynamics of state-specific photoionization and provide a conclusive description of key spectral features in the measured spectra.

Cluster ions composed of a metal complexed with a variety of solvents, particularly those containing alkali metals, form interesting targets of study with ZEKE-PFI techniques.[8] Indeed, their fundamental importance in a wide range of chemical and biological processes, the sodium–potassium pump in the central nervous system and electron solvation being prime examples, has encouraged several experimental and theoretical investigations.[9–11] Experimentally, it is straightforward to produce such cluster ions in sufficient quantities to detect with ZEKE-PFI, and the wavelengths required for their spectroscopic investigations are easily generated with dye lasers.

We have previously reported on the use of moderate resolution ZEKE-PFI spectroscopy to obtain improved ionization potentials (IPs), intermolecular vibrational frequencies, and some structural information for the $Na^+(H_2O)$ and $Na^+(NH_3)$ complexes.[8] High-n Rydberg states of the Na atoms in the complexes were populated by single-photon excitation using tunable UV light for the sodium–water complex. Here we concentrate on the rotational band contours observed at somewhat higher resolution in the ZEKE-PFI spectra of the sodium–water complex, and compare the observed contours to detailed, fully rotationally resolved *ab initio* studies of the ZEKE-PFI process. With their highly anisotropic character and small rotational constants, calculations of the ion rotational distributions for these systems can be expected to be computationally challenging. In what fol-

 © 1998 American Institute of Physics

Downloaded 08 Mar 2006 to 131.215.225.174. Redistribution subject to AIP license or copyright, see http://jcp.aip.org/jcp/copyright.jsp

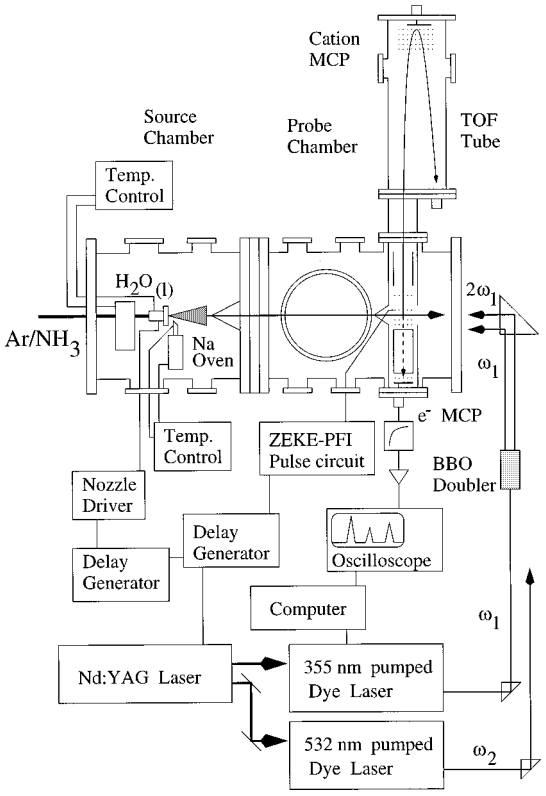

FIG. 1. ZEKE-PFI experimental apparatus. See the text for an explanation.

lows we first present the experimental and theoretical methodologies employed, turning thereafter to a discussion of the results obtained and their implications for further research.

II. EXPERIMENTAL APPROACH

$Na(H_2O)_n$ complexes were formed and studied in a differentially pumped vacuum apparatus comprised of three chambers, an overview of which is presented in Fig. 1. In the first, or source, chamber the complexes were formed in a supersonic jet expansion that was skimmed by a 2-mm-diam skimmer (Beam Dynamics) 5–10 cm downstream of the nozzle, thereby creating an intense, collimated cluster beam. The ZEKE-PFI apparatus was contained in this chamber, to which was attached the third chamber that housed a time-of-flight mass spectrometer (TOFMS). The source chamber was pumped by an unbaffled Varian VHS-10 diffusion pump (DP), the probe chamber by a Varian VHS-6 DP with a water-cooled baffle, and the TOFMS by an Edwards DIFFSTAK 100 DP and water baffle. All three DPs were backed by an Edwards EM2-275 mechanical pump, and typical operating pressures in the source, probe, and TOF chambers were 5×10^{-5}, 5×10^{-7}, and 5×10^{-8} Torr, respectively.

Since sodium and water cannot be coexpanded from the same reservoir, the $Na(H_2O)$ complex was formed in a ''pickup'' source, similar to that used by Hertel and co-workers.[12,13] A supersonic jet containing H_2O seeded in Ar was crossed by an effusive beam of Na atoms. Collisions entrained the Na atoms in the expansion, where a small fraction of them formed complexes. The aperture of the Na oven, heated to 630 K, was placed 5 mm below and 5 mm downstream of the orifice of the pulsed valve (General Valve, series 9, high temperature version, 0.8 mm nozzle diameter). The rotational temperature of the complexes formed by this source was ~100 K.

Sodium–water complexes were formed by expanding 1 atm of water vapor with 1.5 atm of Ar with the argon carrier gas passing through a water reservoir behind the general valve. For these expansion mixtures, the optimum cluster signal was obtained by minimizing the gas flow rate. This was done by keeping the voltage applied to the valve as low as possible. The number of 1:1 complexes ionized per laser shot was ~250. The reservoir and valve were independently heated in the same manner as the sodium oven, described below, with the valve being kept hotter than the reservoir. When the sodium oven was on, it alone heated the valve, the face of which was covered with aluminum foil, to a temperature over 100 °C. The carrier gas tubing leading into the reservoir was Teflon,™ which electrically insulated the reservoir from the chamber.

The stainless-steel sodium oven consisted of two parts, the reservoir and the aperture tube, which were connected by a Swagelok fitting. The reservoir was made by drilling a 12-mm-diam hole in a rod 0.75 in. in diameter and 2 in. long, and welding a Swagelok fitting (0.375 in. diam) to it. The aperture tube was made from a 0.375 in. diam rod which fits into the Swagelok connector. The lower-half of the tube had an outer diameter (o.d.) of 0.375 in. and an inner diameter (i.d.) of 0.290 in., while the rest of the tube had an o.d. of 0.173 in. and an i.d. of 0.125 in. The tip was ground at an angle to minimize the obstruction of the gas flow from the pulsed valve.

The oven's reservoir and aperture tube were heated independently with cartridge resistance heaters (Omega). The sodium reservoir was placed in a hole in an aluminum block, onto which a 0.375 in. o.d. cartridge heater was clamped to the block by another piece of aluminum. The aperture tube was clamped in a hole between two copper plates, as was a 0.25 in. diam 150 W cartridge heater. The oven was supported by a macor bar to prevent heat conduction to the chamber. Typical sodium ovens have much smaller apertures, which must be kept hotter than the reservoir to prevent clogging. While clogging of our large-aperture oven was not a problem, the aperture was kept ~20 °C hotter than the reservoir to keep the part of the oven not in contact with either heating block from getting too cold. Typically, the reservoir was held at 365 °C (Na vapor pressure 0.1 Torr) and the aperture at 385 °C. This gave ~10 h of use when the oven was filled. The cartridge heater for each heating block was connected to a temperature controller (Omega) via an electrical feedthrough, and a chromel–alumel thermocouple was attached to the block, with its wires connected to the temperature controller via a thermocouple feedthrough.

Cluster formation conditions in the pickup source were initially monitored and optimized with nonresonant single photoionization experiments. Later experiments involved both resonant and nonresonant photoionization and ZEKE-PFI photoelectron spectroscopy. The TOFMS was a commercial angular reflectron instrument from R. M. Jordan Co. It houses a multichannel plate (MCP) detector at the end of the 1.1 m flight tube for use as a standard TOFMS and a

Downloaded 08 Mar 2006 to 131.215.225.174. Redistribution subject to AIP license or copyright, see http://jcp.aip.org/jcp/copyright.jsp

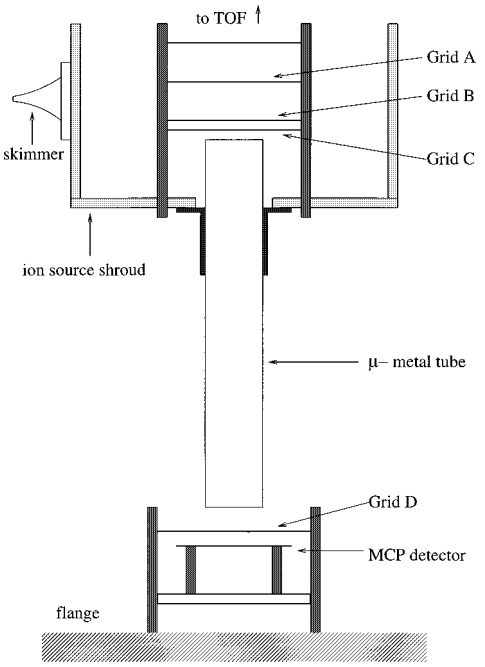

FIG. 2. A close-up schematic cross section of the ZEKE-PFI apparatus outlining the grid patterns and labels of Fig. 1.

second MCP near the ion source for use in the reflectron mode. A Wiley–McClaren ion source, located 50 cm from the pulsed nozzle, was used to achieve spatial and temporal focusing. The extraction field of 315 V/cm and the acceleration field of 3000 V/cm were obtained by holding the repeller plate at 4200 V and the extraction grid at 3800 V. A 4 mm×1 mm skimmer (Beam Dynamics), placed just before the ion source, created a narrow strip of clusters between the extraction grids and limited the amount of gas entering the TOFMS. MCP bias voltages ran from 1800 to 3000 V, depending on the signal strength. The output signal from the detector was sent to an EG&G 9301 preamplifier (×10 gain) and from there to a LeCroy 9400 A digital storage oscilloscope.

The ZEKE apparatus consisted of extraction grids, a μ-metal flight tube, and an MCP detector. The extraction grids were the same as those in the TOFMS, but the electrons were extracted in the direction opposite to the TOF. A third grid was placed 3 mm outside the extraction region to provide additional acceleration for the electrons. The μ-metal flight tube was attached to the ion source to provide shielding against magnetic fields. Finally, the MCP detector was placed on a flange attached to the probe chamber, directly opposite the TOFMS. A schematic of the apparatus outlining the grid patterns is shown in Fig. 2.

Grid B was held at ground, while grid A was connected to the voltage pulse circuitry. The pulser used an inverting CLC 400 op amp. Typically, a -4 V output pulse 10 ms long and having a rise time of $\sim$80 ns was used in the experiments, with a delay time of approximately 2.5 μs. By using different resistors in the circuit smaller pulses can be generated. The offset null of the op amp was used to keep the grid as close to ground as possible when no pulse was applied. Grid C, 3 mm from grid B, was held at a potential of 9 V (provided by batteries) to give the electrons additional acceleration. The μ-metal flight tube was held at this same potential. Grid D, just in front of the detector, was floated because this increased the signal by a factor of $\sim$2. Initially, a set of deflector plates was attached at grid C to ensure that the electrons hit the detector. This was later found to be unnecessary. We achieved excellent signal-to-noise ratios with the present arrangement, but it could be further improved by using either deflector plates or voltage pulses on grid C to eliminate interference from kinetic electrons.

High voltage for the dual MCP ZEKE-PFI detector, typically 1800–2000 V (SRS PS325), was connected to a voltage divider circuit so the appropriate potential difference would be placed across each MCP. The maximum input voltage was 2400 V, at which the voltage across each MCP was 1000 V, the highest allowed value, and the current was 400 mA. The potential difference of 400 V between grid D and the first MCP gives the ZEKE-PFI electrons sufficient energy to generate secondary electrons when they strike the MCP. The anode was held at a potential 200–300 V higher than the last MCP to ensure that the secondary electrons would hit it. This was done by connecting the anode via a low-pass filter to one of the TOF power supply outputs and applying the correct voltage. Since this voltage is too high to connect to the oscilloscope, a high-pass filter was employed so only the ac signal would reach the processing electronics.

In the ZEKE-PFI experiments reported below, a Nd:YAG laser (Continuum YG 681) pumped a dye laser (Lambda Physik FL 3002) at 30 Hz. The FL 3002 bandwidth is nominally 0.2 cm^{-1}. Coumarin 540 A dye was used in the laser, which was pumped at 355 nm and frequency doubled with a BBO crystal. No focusing optics were used. The wavelength of the dye laser was calibrated with a wavemeter (Burleigh WA-4500A) and corrected to its vacuum values. The ZEKE-PFI peak heights were not corrected for the variations of laser power with wavelength, which was sometimes large.

The data collection procedure involved stepping the dye laser's frequency, averaging the ion or electron signal from a few hundred laser shots with the digital oscilloscope, and transferring the data to a personal computer for further processing. The laser scanning and oscilloscope were controlled by the PC, with communication between devices conducted via a GPIB bus (National Instruments). Amplified signals were connected to the oscilloscope with a 50Ω termination and digitized at 10 ns intervals. The oscilloscope was triggered by the signal from a photodiode in mass spectrometry experiments, and by the ionization voltage pulse in ZEKE experiments. Data processing on the PC involved adding the points in the signal peak and subtracting the background. In mass spectrometry experiments, the program located and processed the peaks for any desired number of masses. The processed data was stored in a file on the PC's hard drive, and, for most experiments, the entire oscilloscope wave form at each laser step was stored as well. Digital delay generators (SRS DG-535) were used to synchronize the laser pulses with the molecular beam pulses. The General Valve driver was operated in an internal trigger mode at 30 Hz to control the timing sequence, with the valve driver triggering a DG-

Downloaded 08 Mar 2006 to 131.215.225.174. Redistribution subject to AIP license or copyright, see http://jcp.aip.org/jcp/copyright.jsp

535 which, after the appropriate delay, triggered another DG-535 that fired the Nd:YAG laser and the ZEKE pulse circuit.

III. THEORETICAL APPROACH

A. Differential cross section

Photoionization of the $7a_1(3sa_1)$ orbital of the $\tilde{X}\,^2A_1$ ground state of the $Na(H_2O)$ complex leads to the $\tilde{X}\,^1A_1$ ground state of the ion. For simplicity, we assume C_{2v} molecular symmetry for both the neutral and ionic species, even though, for the neutral, some authors find a shallow double minimum potential with respect to the out-of-plane intermolecular bending mode of the complex.[13] Under collision-free conditions, the rotationally resolved differential cross section for single-photon ionization of a rotational level of the ground state of a molecule by linearly polarized light can be written as[14]

$$\frac{d\sigma}{d\Omega}=\frac{\sigma}{4\pi}[1+\beta P_2(\cos\,\theta)], \tag{1}$$

where σ is the total cross section, β the asymmetry parameter, and $P_2(\cos\theta)$ the second Legendre polynominal. The total cross section σ and asymmetry parameter β have the form

$$\sigma\propto\sum_{\substack{lm\\M_{J_i}M_{J_+}}}\rho_{M_{J_i}M_{J_i}}|C_{lm}(M_{J_i}M_{J_+})|^2, \tag{2}$$

and

$$\beta=\frac{5}{\sigma}\sum_{\substack{ll'm\\M_{J_i}M_{J_+}}}(-1)^m(2l+1)(2l'+1)\rho_{M_{J_i}M_{J_i}}\times C_{lm}(M_{J_i}M_{J_+})C^*_{l'm}(M_{J_i}M_{J_+})\begin{pmatrix}l & l' & 2\\ m & -m & 0\end{pmatrix}\times\begin{pmatrix}l & l' & 2\\ 0 & 0 & 0\end{pmatrix}, \tag{3}$$

where $\rho_{M_{J_i}M_{J_i}}$ is the population of the M_{J_i} sublevel of the ground state and $C_{lm}(M_{J_i}M_{J_+})$ is the coefficient for photoionization of the M_{J_i} level of the ground state leading to the M_{J_+} level of the ion. Note that each M_J channel is treated independently in this formulation. By employing symmetry-adapted angular functions and making use of the properties of 3-j symbols, Lee *et al.* have derived an expression for $C_{lm}(M_{J_i}M_{J_+})$ for molecules with C_{2v} symmetry.[14] $C_{lm}(M_{J_i}M_{J_+})$ has the form

$$C_{lm}(M_{J_i}M_{J_+})=\sqrt{\frac{4\pi}{3}}\frac{1}{2}[(2J_i+1)(2J_++1)(2N_i+1)(2N_++1)(2S_i+1)]^{1/2}\sum(-1)^Q(2N_t+1)\begin{pmatrix}S_+ & \frac{1}{2} & S_i\\ M_{S_+} & m_\sigma & -M_{S_i}\end{pmatrix}\times\begin{pmatrix}N_+ & S_+ & J_+\\ M_{N_+} & M_{S_+} & -M_{J_+}\end{pmatrix}\begin{pmatrix}N_i & S_i & J_i\\ M_{N_i} & M_{S_i} & -M_{J_i}\end{pmatrix}\begin{pmatrix}N_+ & N_i & N_t\\ -M_{N_+} & M_{N_i} & m_t\end{pmatrix}\begin{pmatrix}N_t & 1 & l\\ -m_t & \mu_0 & m\end{pmatrix}\times a_{N_ir_iK_i}a_{N_+r_+K_+}\tilde{I}^{\gamma q}_{hl\lambda\mu}(\Lambda_f\Sigma_f)b^{\gamma q}_{hl\lambda}(\Lambda_f\Sigma_f)[1+(-1)^{\Delta p+\Delta N+l+1}]\left[\begin{pmatrix}N_+ & N_i & N_t\\ -K_+ & K_i & K_t\end{pmatrix}\begin{pmatrix}N_t & 1 & l\\ -K_t & \mu & \lambda\end{pmatrix}+(-1)^{p_+}\begin{pmatrix}N_+ & N_i & N_t\\ K_+ & K_i & K_t\end{pmatrix}\begin{pmatrix}N_t & 1 & l\\ -K_t & \mu & \lambda\end{pmatrix}\right], \tag{4}$$

$$Q=\Delta N+\Delta M_J-S_i+M_{S_i}-\mu_0-m+M_{N_+}+K_i-1/2 \tag{5}$$

and

$$\tilde{I}^{\gamma q}_{hl\lambda\mu}(\Lambda_f\Sigma_f)=\langle\lambda_+q_+\lambda_eq_e|\Lambda_f\rangle\times\langle M_{S_+}m_\sigma|\Sigma_f\rangle I^{\gamma q}_{hl\lambda\mu}(\Lambda_f\Sigma_f), \tag{6}$$

with $\Delta p=p_+-p_i$, $\Delta M_J=M_{J_+}-M_{J_i}$, $\Delta N=N_+-N_i$, where the summation in Eq. (4) goes over all possible indices. Note that subscripts i and $+$ of these equations denote the quantum numbers for the ground and ionic states, respectively. In Eq. (4), N is the total angular momentum (exclusive of spin), K is its projection on the z axis, p is the parity of the rotational wave function, N_t is the angular momentum transfer, l is an angular momentum component of the photoelectron, λ is its projection along the molecular z axis, and μ is the light polarization index in the molecular frame. Also, γ is one of the irreducible representations of the molecular point group, q is a component of this representation, h distinguishes between different bases for the same irreducible representation corresponding to the same value of l, and $I^{\gamma q}_{hl\lambda\mu}(\Lambda_f\Sigma_f)$ is the partial wave photoelectron matrix element for each dipole-allowed multiplet-specific final-state wave function $|\Lambda_f\Sigma_f\rangle$ (ion+photoelectron).[7] Furthermore, in Eq. (4) the coefficients $a_{N\tau K}$ are used for the expansion of the asymmetric top wave functions and are determined by diagonalizing the rigid rotor Hamiltonian

$$H_r=\frac{J_x^2}{2I_x}+\frac{J_y^2}{2I_y}+\frac{J_z^2}{2I_z} \tag{7}$$

in the basis of the symmetric top eigenfunctions where $\tau=K_a-K_c$, K_a and K_c being the projections of total angular

Downloaded 08 Mar 2006 to 131.215.225.174. Redistribution subject to AIP license or copyright, see http://jcp.aip.org/jcp/copyright.jsp

momentum along the a and c axes. Finally, the $b^{\gamma q}_{hl\lambda}(\Lambda_f\Sigma_f)$ coefficients are introduced to combine spherical harmonics $Y_{l\lambda}(\hat{k})$ into generalized harmonics $X^{\gamma q}_{hl\lambda}(\hat{k})$ as

$$X^{\gamma q}_{hl\lambda}(\hat{k}) = b^{\gamma q}_{hl\lambda} Y_{l\lambda}(\hat{k}) + b^{\gamma q}_{hl-\lambda} Y_{l-\lambda}(\hat{k}) \tag{8}$$

in the body-fixed frame. The coefficients $b^{\gamma q}_{hl\lambda}$ for C_{2v} symmetry have been given by Burke *et al.*[15] Here we used the generalized harmonics $X^{\gamma q}_{hl\lambda}(\hat{k})$ as bases for the irreducible representation of the molecular point group. Note that the above formulations are also suitable for photoionization of symmetric tops except that the $a_{N\tau K}$ of Eq. (4) become unity for both the ground and ionic states.

B. Photoelectron matrix element

A central quantity characterizing molecular photoionization dynamics is the matrix element for photoejection of an electron from a bound orbital $\phi_i^{\gamma' q'}$ into a continuum orbital $\Psi^{(-)}_{f,\mathbf{k}}(\mathbf{r})$. The multipole composition of the molecular ion potential exerts a strong influence on the character of this matrix element. The partial wave components $\psi^{(-)\gamma q}_{khlm}$ of $\Psi^{(-)}_{f,\mathbf{k}}(\mathbf{r})$ are defined by an expansion in generalized harmonics about $\hat{\mathbf{k}}$ of the photoelectron[7]

$$\Psi^{(-)}_{f,\mathbf{k}}(\mathbf{r}) = \left(\frac{2}{\pi}\right)^{1/2} \sum_{lm} i^l \psi^{(-)\gamma q}_{khlm}(\mathbf{r}) X^{*\gamma q}_{hlm}(\hat{\mathbf{k}}). \tag{9}$$

Here $\mathbf{k}$ is the momentum of the photoelectron and $(-)$ denotes incoming-wave boundary conditions. Single-center expansions of $\psi^{(-)\gamma q}_{khlm}(\mathbf{r})$ and $\phi_i^{\gamma' q'}(\mathbf{r}')$, e.g.,

$$\psi^{(-)\gamma q}_{khlm}(\mathbf{r}) = \sum_{l'\lambda} g^{\gamma q}_{hlm,l'\lambda}(k,r) \mathscr{D}^{l'}_{m\lambda} X^{\gamma q}_{hl'\lambda}(\hat{\mathbf{r}}'), \tag{10}$$

define partial wave photoelectron matrix elements $I^{\gamma q}_{hl\lambda\mu}$ of Eq. (6) in the molecular frame for ionization out of the orbital $\phi_i^{\gamma' q'}(\mathbf{r}')$, i.e.,

$$I^{\gamma q}_{hl\lambda\mu} = \sum_{l',l_0\lambda_0} \langle g^{\gamma q}_{hlm,l'\lambda}(k,r) X^{\gamma q}_{hl'\lambda}(\hat{\mathbf{r}}') \times |rY_{1\mu}(\hat{\mathbf{r}}')| \phi^{\gamma' q'}_{ih'l_0}(r) X^{\gamma' q'}_{h'l_0\lambda_0}(\hat{\mathbf{r}}')\rangle, \tag{11}$$

where $\mathscr{D}^l_{m\lambda}$ is a rotational matrix in Edmonds' notation.[16]

C. Parity selection rules

Parity selection rules govern changes of rotational angular momentum between the neutral and ion upon ionization of specific rovibronic levels. An obvious selection rule

$$\Delta N + \Delta p + l = \text{odd}, \tag{12}$$

can be easily obtained from Eq. (3). This is the same as for photoionization of the Hund's case (b) states of linear molecules, since we use a Hund's case (b) basis.[17] However, this rule is not particularly useful for the nonlinear system of interest here since each rotational quantum number N is associated with $2N+1$ sublevels, designated as N_{K_a,K_c}, and each N_{K_a,K_c} level has its own parity index p. A transformation from the ambiguous selection rule above to a more specific one with respect to K_a and K_c is therefore desirable.

We choose a left-handed coordinate system for the molecular internal x, y, and z axes, with the molecular z axis lying along the highest symmetry axis. Using the symmetry properties of asymmetric tops, it can be shown that ΔK_η is even (odd) when $\Delta N + \Delta p$ is even (odd). Here η is the principal axis lying along the molecular x axis and K_η is the projection of the total angular momentum along that axis. Thus, from Eq. (12) we have the selection rule[18]

$$\Delta K_\eta + l = \text{odd}. \tag{13}$$

In this study of the $Na(H_2O)$ complex, the molecular z axis is chosen to coincide with the C_2 symmetry axis, while the x axis lies in the plane of the molecule (ion). Thus, the molecular x, y, and z axes coincide with the b, c, and a axes, respectively. Therefore, the selection rule of Eq. (13) becomes

$$\Delta K_b + l = \text{odd}. \tag{14}$$

There are three corresponding dipole-allowed continuum channels, namely, ka_1, kb_1, and kb_2 for photoionization of the a_1 orbital of the ground state of $Na(H_2O)$. On the basis of the conservation of total angular momentum upon ionization, the $\mu+\lambda$ value for each of the continuum channels must be even. Furthermore, by making use of the properties of 3-j symbols, Eq. (4) can be rewritten to yield $\mu+\lambda = \Delta K_a$. Hence, we have

$$\Delta K_a = \text{even}. \tag{15}$$

For the symmetry properties of the asymmetric top,[18] Eq. (15) leads to

$$\Delta K_b + \Delta K_c = \text{even}. \tag{16}$$

From Eqs. (14) to (16), we conclude that both type a (ΔK_a = even and ΔK_c = odd) and type b (ΔK_a = even and ΔK_c = even) transitions are allowed, but the type c (ΔK_a = odd and ΔK_c = even) and the other type b (ΔK_a = odd and ΔK_c = odd) transitions are forbidden. Furthermore, Eq. (14) shows that the allowed type b transitions arise from odd partial wave contributions to the photoelectron matrix element, whereas type a transitions are due to even partial wave contributions.

D. Numerical details

The ground state wave function of $Na(H_2O)$ used here is obtained at the self-consistent-field (SCF) level at the equilibrium geometry[19] of $R(\text{Na–O}) = 2.355$ Å, $R(\text{O–H}) = 0.950$ Å, and $\theta(\text{H–O–H}) = 106.9°$. The basis set consists of a $[4s2p]$ contraction of the $(14s7p)$ primitive Cartesian functions of Huzinaga and Arnau,[20] augmented with one p ($\alpha = 0.12$) and two d ($\alpha = 0.68$ and 0.135) functions on the Na atom. On the oxygen atom, we used a $[5s4p]$ contraction of the $(10s6p)$ primitive Gaussian functions of Dunning,[21] augmented with two d ($\alpha = 1.2188$ and 0.3611) functions. On the hydrogen atom, we used a $[3s]$ contraction of the $(4s)$ primitive Gaussian functions of Dunning,[21] augmented with one s ($\alpha = 0.075$) and two p ($\alpha = 1.12$ and 0.1296) functions. On the center of mass, these bases were further augmented with three s ($\alpha = 0.2$, 0.05, and 0.02), two p (α

Downloaded 08 Mar 2006 to 131.215.225.174. Redistribution subject to AIP license or copyright, see http://jcp.aip.org/jcp/copyright.jsp

$=0.08$ and 0.025), and two d ($\alpha=0.08$ and 0.025) Gaussian functions. The total SCF energy in this basis was $-237.433\,449$ a.u.

The procedures for obtaining the photoelectron continuum orbitals used in these studies have been discussed previously. Briefly, the photoelectron orbitals ϕ_k are obtained using an iterative procedure, based on the Schwinger variational principle, to solve the Lippmann–Schwinger equation.[7] This procedure begins by approximating the static-exchange potential of the molecular ion by a separable form

$$U(\mathbf{r},\mathbf{r}')=\sum_{i,j}\langle\mathbf{r}|U|\alpha_i\rangle(U^{-1})_{ij}\langle\alpha_j|U|\mathbf{r}'\rangle, \tag{17}$$

where the matrix U^{-1} is the inverse of the matrix with elements $U_{ij}=\langle\alpha_i|U|\alpha_j\rangle$ and the α's are discrete basis functions such as Cartesian Gaussian functions. U is twice the static-exchange potential with the long-range Coulomb potential removed. The Lippmann–Schwinger equation with this separable potential $U(\mathbf{r},\mathbf{r}')$ can be readily solved yielding approximate photoelectron orbitals $\phi_k^{(0)}$. These solutions can be improved iteratively to yield converged orbitals to the Lippmann–Schwinger equation containing the full static-exchange potential. In this study, up to nine iterations were used to provide converged results.

We assume there is no spin exchange taking place during the jet-cooled expansion of the room-temperature water source. Therefore, the *ortho* (antisymmetric) to *para* (symmetric) ratio for jet-cooled NaH_2O is 3:1. The population distribution was normalized to the statistical ratio for the symmetric and antisymmetric species with respect to their lowest rotational energy levels 0_{00} and 1_{01}, respectively.

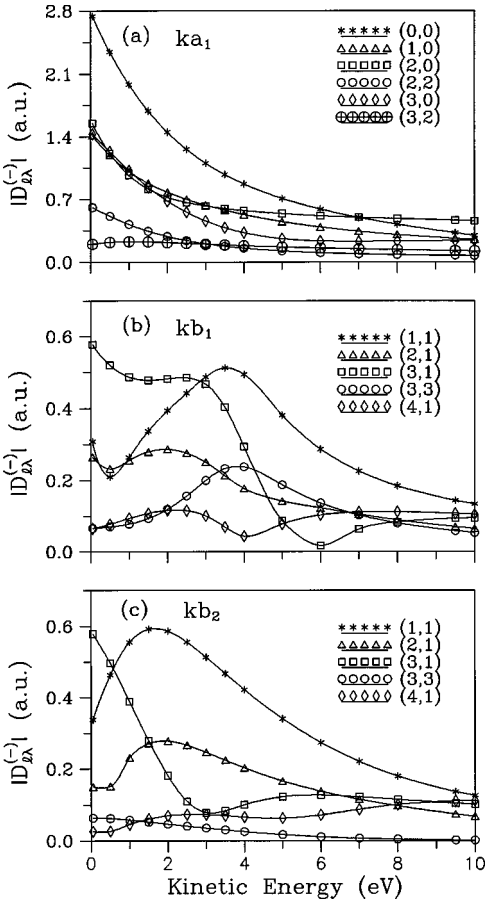

FIG. 3. Magnitude $|D_l^{(-)}|$ of the partial wave components of the photoelectron matrix element for photoionization of the $\tilde{X}\,^2A_1$ $(3sa_1)$ state of NaH_2O: (a) $3sa_1\rightarrow ka_1$, (b) $3sa_1\rightarrow kb_1$, and (c) $3sa_1\rightarrow kb_2$.

IV. RESULTS AND DISCUSSION

A. Body-frame dynamical quantities

A single-center expansion shows that the $3sa_1$ orbital of the ground state of $Na(H_2O)$ has 90.97% s, 6.64% p, 1.14% d, and 0.52% f character about the center of mass and that the $3s$ valence electron of the Na is only slightly delocalized. On the basis of atomiclike propensity rules, the p wave should be the dominant component of the photoelectron matrix element for ionization of this orbital. However, our calculated photoelectron matrix elements show a very different and molecular behavior. Figure 3 shows the magnitude $|D_l^{(-)}|$ of the (incoming-wave normalized) partial wave dipole amplitude as a function of photoelectron kinetic energy for the $3sa_1\rightarrow ka_1$ [Fig. 3(a)], $3sa_1\rightarrow kb_1$ [Fig. 3(b)], and $3sa_1\rightarrow kb_2$ [Fig. 3(c)] channels for ionization of this $3sa_1$ orbital. The angular momentum components of the photoelectron matrix element are labeled by (l,λ) where λ is the projection of the l partial wave along the principal axis. Significant features of Fig. 3 include: (i) an unusually strong s wave component in the ka_1 photoelectron continuum, (ii) strong l mixing among the p, d, and f partial waves of the photoelectron at low energies in the ka_1 channel, (iii) the minimum in the p wave of the kb_1 continuum near threshold, (iv) the behavior of the p wave in the kb_2 channel at threshold, (v) minima in the (3,1), (4,1) components of the kb_1 and kb_2 channels, and (vi) a prevalent p wave only at larger kinetic energies in the kb_1 and kb_2 channels.

The significant s, d, and f wave contributions to the photoionization matrix element, particularly near threshold, reflect the strong anisotropy of the molecular ion potential. Only at higher kinetic energies does the p wave become prevalent. While a Cooper minimum is not seen in the p wave of either the b_1 or b_2 channels, these partial wave photoionization matrix elements bear the fingerprint of the Cooper zero seen in the Na cross section.[22] More specifically, the minimum in the p wave of the b_1 continuum is not a Cooper minimum since the corresponding principal-value (standing-wave normalized) dipole amplitude $D_{l\lambda}^P$ does not change sign within the energy range shown. Due to l mixing in molecular systems, the position of a Cooper zero in $D_{l\lambda}^P$ may differ from the location of a minimum in $|D_{l\lambda}^{(-)}|$. The minima associated with the (3,1) and (4,1) components of the photoionization matrix element are, however, true Cooper minima. Actual sign changes are seen in the principal-value form of these dipole matrix components.

B. ZEKE photoelectron spectra

Figure 4 shows our measured [Fig. 4(a)] and calculated [Fig. 4(b)] ZEKE photoelectron spectra for ionization of the $3sa_1$ orbital of the $\tilde{X}\,^2A_1$ state of NaH_2O. The measured

Downloaded 08 Mar 2006 to 131.215.225.174. Redistribution subject to AIP license or copyright, see http://jcp.aip.org/jcp/copyright.jsp

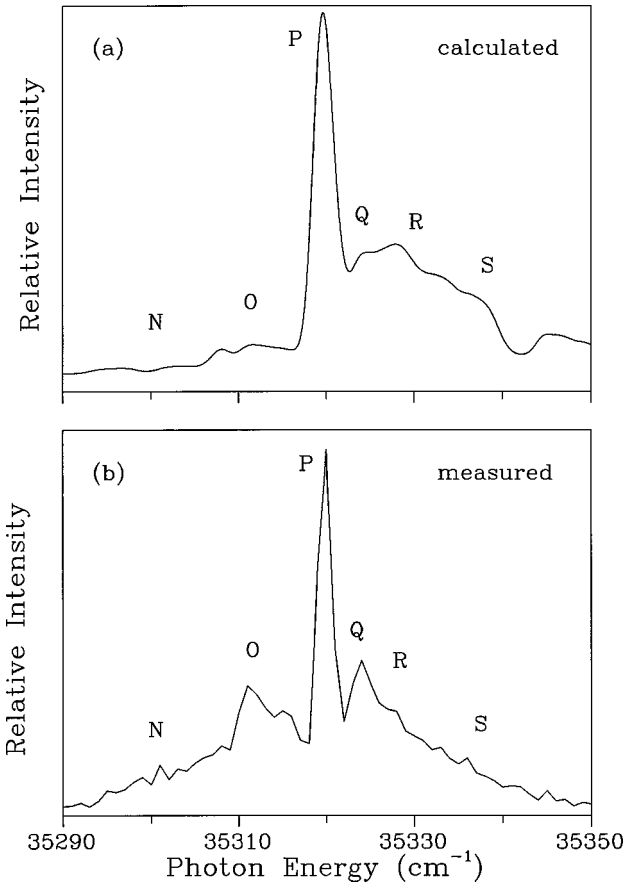

FIG. 4. (a) Calculated and (b) measured ZEKE-PFI photoelectron spectra at a rotational temperature of 100 K. The calculated spectrum assumed rotational constants calculated at equilibrium geometry. See the text.

spectrum is recorded with 1 cm^{-1} laser steps. Similar rotational contours are observed for states with one or more quanta in the pseudodiatomic stretch of the cation, reflecting the small geometry changes associated with excitation of the intermolecular vibrational degrees of freedom. The calculated spectra were obtained for a photoelectron energy of 50 meV and were convoluted with a Gaussian detector function having a full width at half-maximum (FWHM) of 2.2 cm^{-1}. The rotational constants used were derived from the calculated geometries of Ref. 19. For $Na(H_2O)$, these are $A=14.157$, $B=0.280$, and $C=0.275$ cm^{-1} and $A^+=14.157$, $B^+=0.309$, and $C^+=0.296$ cm^{-1} for $Na(H_2O)^+$. Comparison of the measured ZEKE photoelectron spectra with spectra calculated over a wide temperature range suggests that the rotational temperature in these experiments is about 100 K, similar to the vibrational temperature estimated from the intensities of intermolecular stretching and bending hot bands in the ZEKE-PFI spectra.[8] The spectrum shown in Fig. 4(a) was calculated at this temperature.

While we do not label specific rotational transitions due to the very large number of such transitions that contribute to these spectra, the dominant peak in the measured and calculated spectra belongs to *P* branch transitions. The intensity of this peak is due to a bandhead. The *Q*, *R*, and *S* branches are spread to the blue of this peak while the *O* branch lie to its red. Agreement between the measured and calculated spectra is encouraging except for the *O* branch where the calculated spectrum shows a much weaker intensity. This discrepancy between calculated photoelectron spectra and rotational intensity profiles derived from PFI spectra for negative ΔN transitions has been seen in a wide range of systems and is generally attributed to field-induced rotational autoionization.[23]

Analysis of the calculated spectrum indicates that $|\Delta N|=0-4$ transitions contribute 13%, 62%, 15%, 7%, and 3% of the total cross section, respectively. The dominance of the $P(28\%)$ and $R(34\%)$ branches can be readily understood from the photoelectron matrix elements of Fig. 3(a) which show a very strong *s*-wave component. On the basis of angular momentum considerations, this *s* wave ($l=0$) is responsible for the strong $\Delta N=\pm 1$ transitions. This behavior is quite unusual for photoionization of an orbital with predominant *s* character ($\sim 91\%$) where atomiclike propensity rules would suggest a strong *p*-wave photoelectron matrix element.

With its large Na···O bond length, one would expect photoionization of $Na(H_2O)$ to occur mainly along the *a* principal axis. Indeed, an analysis shows that more than 98% of the cross section is associated with transitions possessing no change in the angular momentum about K_a, i.e., $\Delta K_a=0$ and only about 2% of the cross section is from $\Delta K_a=\pm 2$ transitions. Note that $\Delta K_a=\pm 1$ transitions are dipole forbidden. Furthermore, a similar rotational analysis indicates that $|\Delta K_c|=0-4$ transitions account for about 11%, 63%, 16%, 7%, and 3% of the total cross section, respectively. On the basis of the parity selection rules of Eqs. (14)–(16), transitions with $\Delta K_c=odd$ arise from even l partial waves of the photoelectron matrix element whereas transitions with $\Delta K_c=even$ are from odd partial waves. Even partial waves of the photoelectron matrix element hence account for about 70% of the total cross section, i.e., type *a* transitions. This contribution is entirely molecular in nature for photoionization of an orbital with 91% *s* character. This strong nonatomiclike behavior is probably also due to depletion of the *p* wave of the kb_1 and kb_2 continua near threshold (see the above section). This depletion of the *p* wave enhances the relative contributions of the even waves.

To explore the utility of studies of this kind in elucidating the molecular structure of neutral and charged clusters, it is instructive to see how changes in the intermolecular geometry may influence the contour of the calculated PFI spectra. With such small *B* and *C* rotational constants (the *A* constant does not play a role in determining the ''end-over-end'' rotational spacing), one should bear in mind that a slight change in relative *B* and *C* values in the neutral and cation can lead to dramatic change in the spectral profile since at a temperature of 100 K more than 300 transitions contribute to the spectrum. The *P* branch peak intensity and its underlying bandhead make this an interesting case to study. Figure 5 shows the calculated spectrum for slight changes in rotational constants to $B=0.295$ and $C=0.283$ cm^{-1} for $Na(H_2O)$ and $B^+=0.298$ and $C^+=0.286$ cm^{-1} for $Na(H_2O)^+$ but with the same *A* and A^+ rotational constants and photoelectron matrix elements. This change reflects about a 2% decrease in the Na···O bond

Downloaded 08 Mar 2006 to 131.215.225.174. Redistribution subject to AIP license or copyright, see http://jcp.aip.org/jcp/copyright.jsp

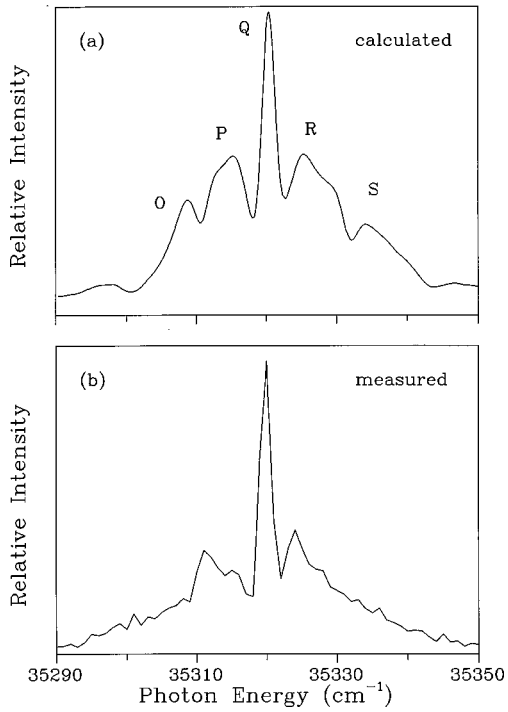

FIG. 5. (a) Calculated and (b) measured ZEKE-PFI photoelectron spectra at a rotational temperature of 100 K. The calculated spectrum assumed slightly modified rotational constants. See the text for a discussion.

length from 2.36 to 2.32 Å for the NaH_2O complex, and a similar increase in the pseudo-diatomic bond length for the cation. These new rotational constants result in a shift of only about 2 cm^{-1} in the location of the peak of rotational contour. However, due to the relative change in the lower and upper state constants, the calculated spectrum shows a dramatically different spectral profile. With these changes in the B and C rotational constants, it is now the Q branch which dominates the peak intensity even though it only contributes about 13% of the cross section since the similarity of the rotational constants in the lower and upper states preclude the formation of P- or R-branch bandheads. The apparent agreement between these calculated and measured spectra is quite good.

Are the actual rotational constants close to these modified constants? Comparison of experimental and theoretical constants for such clusters can have large uncertainties due to the extensive vibrational averaging which is present in simple fits to spectra, but which would require an accurate knowledge of the global intermolecular potential energy surface to be included in theoretical treatments. In this context, both the intermolecular stretching and out-of-plane bending modes,[13] which were not considered in these calculations, may contribute to such uncertainties in the rotational constants.

There are several reasons the interpretation of the data presented in Fig. 4 is preferred. First, the most intense peak in the measured spectrum belongs to a P-branch bandhead and that the wing to its red is an O-branch enhanced by field-induced rotational autoionization. All of the theoretical studies performed to date predict a shrinkage of the bond length upon ionization similar to or larger than that used here—regardless of the level of theory or the computational approach employed.[19,24] Further, in resonance enhanced multiphoton ionization studies of the similar $Na(NH_3)$ complex that obey more restrictive optical selection rules,[8,25] rotational contours within the excited $\tilde{A}$ state clearly demand a bond length contraction relative to the neutral ground state. Finally, in high-resolution multiphoton ZEKE-PFI studies of $Na(NH_3)$, rotationally resolved spectra again require a sizable bond length contraction upon ionization, and the resulting change in the rotational constants is in good agreement with theory.[26] Unambiguous clarification of these issues in $Na(H_2O)$ awaits higher spectral resolution experiments.

C. Rotationally resolved ZEKE photoelectron spectra

While rotationally resolved spectra are well beyond the resolution of these measured ZEKE spectra, they are an essential step in the calculation of the rotational profiles shown in Fig. 5 and may also provide valuable insight into the photoionization dynamics. To illustrate such underlying dynamics in $Na(H_2O)$, and to provide a guide for future high-resolution spectroscopy and ZEKE-PFI study of this cluster, we now show calculated rotationally resolved ZEKE photoelectron spectra from single rotational levels of this system. We choose initial levels with $K_a=0$ for these purposes. Figure 6 shows the calculated ZEKE photoelectron spectra for ionization out of the 0_{00} [Fig. 6(a)], 1_{01} [Fig. 6(b)], 2_{02} [Fig. 6(c)], 3_{03} [Fig. 6(d)], and 10_{010} [Fig. 6(e)] rotational levels. Each transition is labeled by $N^+_{K_a^+K_c^+}$ where K_a^+ and K_c^+ are the projection of the angular momentum N^+ along the principal a and c axes, respectively. The transitions with $\Delta K_a=\pm 2$ are too weak to show here.

On the basis of parity selection rules, transitions associated with $\Delta K_c=odd$ (cross-hatched bars) arise from even partial wave contributions to the photoelectron matrix element, whereas those with $\Delta K_c=even$ (solid bars) are from the odd partial waves. Obviously, even partial wave contributions dominate for photoionization of all rotational levels in Fig. 6. In addition, $\Delta N=1$ transitions are the most intense peaks arising from even waves (primarily via the s wave). An interesting feature of these results is the relative intensities for the $\Delta N=\pm 1$ transitions. As the initial rotational level of the neutral approaches the high N limit, both $\Delta N_a=\pm 1$ transitions have almost the same intensities [see Fig. 6(e)]. At the lower N levels, angular momentum coupling between N and l is more critical and the spectral profiles show more distinct asymmetries.

Figure 7 shows rotationally resolved ZEKE photoelectron spectra for photoionization of the 1_{11} [Fig. 7(a)], 2_{12} [Fig. 7(b)], 3_{13} [Fig. 7(c)], and 10_{110} [Fig. 7(d)] levels of the ground state $Na(H_2O)$. Comparison of the results of Figs. 6 and 7 illustrates the effect of the angular momentum K_a on the photoionization dynamics. The $\Delta N_a=\pm 1$ transitions are dominant in both cases, as discussed above. The most striking difference is that for the levels with $K_a=1$, each ΔN transition leads to two nearly degenerate rotational levels of the ion, which arise from either even or odd partial wave components of the photoelectron. Even wave contributions are shown by the cross-hatched bars and odd waves by solid

Downloaded 08 Mar 2006 to 131.215.225.174. Redistribution subject to AIP license or copyright, see http://jcp.aip.org/jcp/copyright.jsp

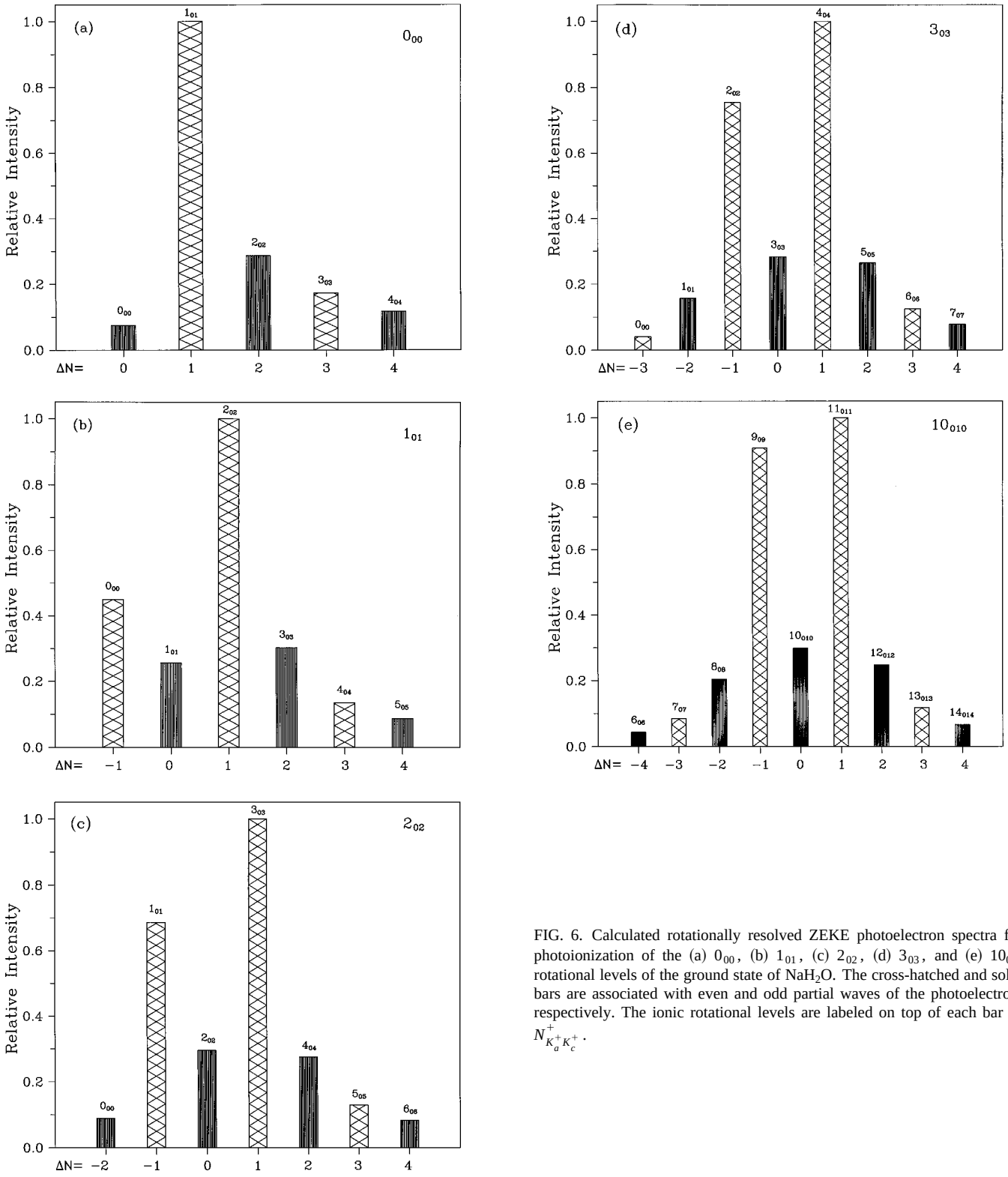

FIG. 6. Calculated rotationally resolved ZEKE photoelectron spectra for photoionization of the (a) 0_{00}, (b) 1_{01}, (c) 2_{02}, (d) 3_{03}, and (e) 10_{010} rotational levels of the ground state of NaH_2O. The cross-hatched and solid bars are associated with even and odd partial waves of the photoelectron, respectively. The ionic rotational levels are labeled on top of each bar as $N^+_{K_a^+K_c^+}$.

bars. At the higher N levels, these spectral profiles are very similar. For low N rotational levels, however, the spectral profiles are very different for photoionization of the $K_a=0$ and $K_a=1$ levels. For example, a very intense transition occurs for $\Delta N=0$ for the 1_{11} level whereas this transition is much weaker for the 1_{01} level. This illustrates the subtle effect of the angular momentum K_a. This effect is important only in the case of smaller N levels and has its origin in the 3-j symbol.

V. CONCLUSIONS

Detailed theoretical and experimental studies of the ZEKE-PFI photoelectron spectroscopy of the $Na(H_2O)$ com-

Downloaded 08 Mar 2006 to 131.215.225.174. Redistribution subject to AIP license or copyright, see http://jcp.aip.org/jcp/copyright.jsp

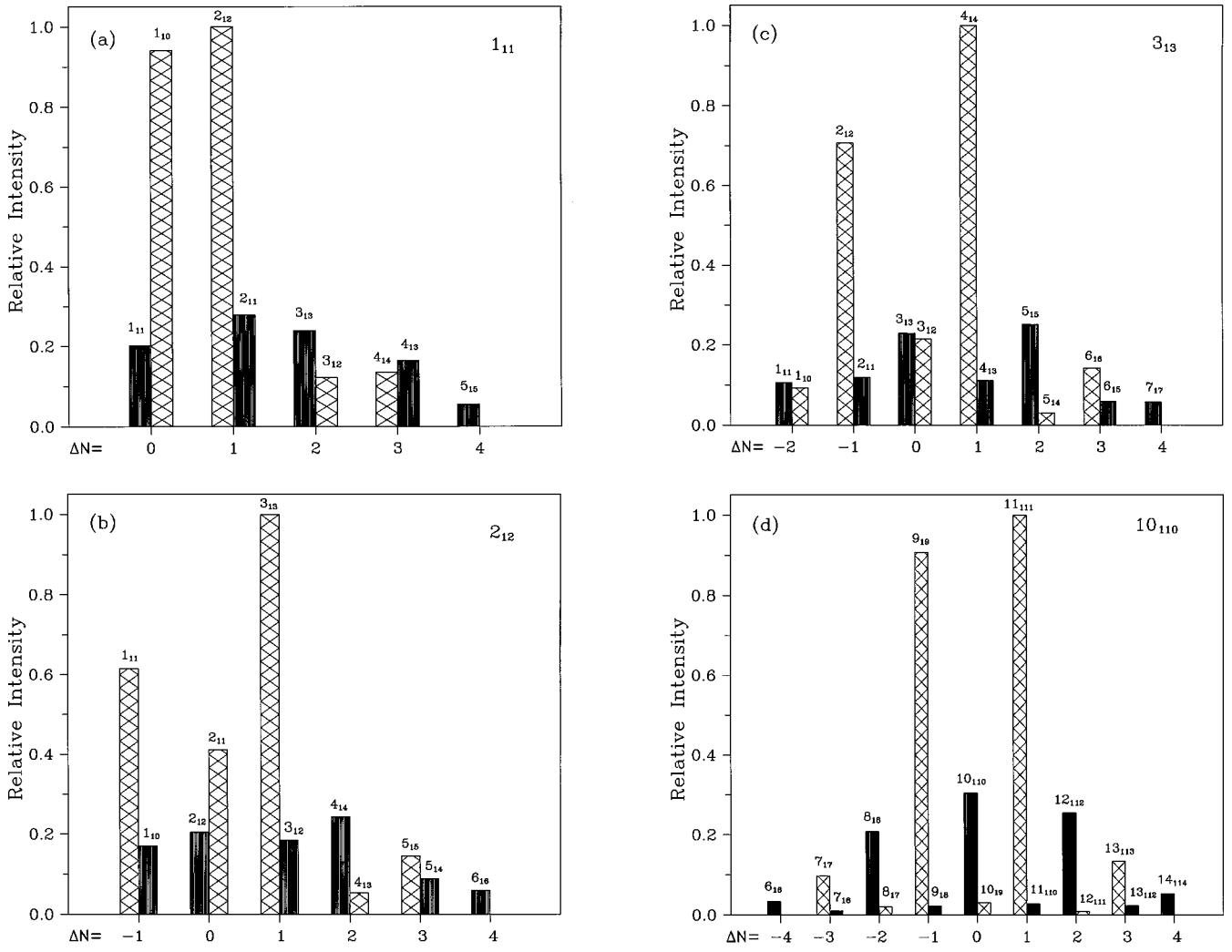

FIG. 7. Calculated rotationally resolved ZEKE photoelectron spectra for photoionization of the (a) 1_{11}, (b) 2_{12}, (c) 3_{13}, and (d) 10_{110} rotational levels of the ground state of NaH_2O. The cross-hatched and solid bars are associated with even and odd partial waves of the photoelectron, respectively. The ionic rotational levels are labeled on top of each bar as $N^+_{K_a^+K_c^+}$.

plex are presented. Clusters of this type not only provide interesting model systems of the solvation process, but their strong anisotropies and small rotational constants result in rich photoionization dynamics. The nonatomiclike nature of the photoionization process is clear in the theoretical calculations, and should be readily observable once fully rotationally resolved experimental ZEKE-PFI spectra are obtained. Several routes to such spectra can be envisioned. For example, laser vaporization sources offer much colder rotational temperatures, and would dramatically decrease the number of states contributing to the ZEKE-PFI photoelectron signal. Single-photon excitation with transform-limited pulses should also result in better resolution, although the small rotational constants of $Na(H_2O)$ and other molecular clusters will render such experiments very difficult indeed.

Alternatively, multiphoton ZEKE-PFI studies can be performed in which one laser is used to select individual eigenstates of the neutral percursor, which are subsequently excited to Rydberg levels and pulse-field ionized. For clusters containing sodium or other alkali metal atoms, the first spectroscopic step could involve either electronic excitation of the metal itself or vibrational excitation of intramolecular modes within the solvent molecules. Experiments of this type would not only provide rotationally resolved spectra to be compared with detailed theoretical calculations, but would also permit large regions of the intermolecular potential energy surfaces of both the neutral and cation to be mapped in great detail. Such efforts are presently underway for the $Na(NH_3)$ and $Na(H_2O)$ complexes.

ACKNOWLEDGMENTS

This work was supported by grants from the Air Force Office of Scientific Research and the Office of Health and Environmental Research of the U.S. Department of Energy. We also acknowledge use of the resources of the Jet Propulsion Laboratory/California Institute of Technology CRAY J916/8-4096 supercomputer. This work is also supported by NASA (Grant Nos. NAGW-2813 and -1955) and the National Science Foundation (CHE-9415488). Initial instrumentation funding was provided by the David and Lucille Packard Foundation.

Downloaded 08 Mar 2006 to 131.215.225.174. Redistribution subject to AIP license or copyright, see http://jcp.aip.org/jcp/copyright.jsp

[1] R. N. Compton and J. C. Miller, in *Laser Application in Physical Chemistry*, edited by D. K. Evans (Dekker, New York, 1988).
[2] K. Müller-Dethlefs and E. W. Schlag, Annu. Rev. Phys. Chem. **42**, 109 (1991).
[3] K. Müller-Dethlefs, E. W. Schlag, E. R. Grant, K. Wang, and V. McKoy, Adv. Chem. Phys. **90**, 1 (1995).
[4] R. T. Wiedman and M. G. White, in *High Resolution Laser Photoionization and Photoelectron Studies*, edited by I. Powis, T. Baer, and C. Y. Ng (Wiley, New York, 1995).
[5] K. Wang and V. McKoy, Annu. Rev. Phys. Chem. **46**, 275 (1995).
[6] K. Wang and V. McKoy, in Ref. 4.
[7] R. R. Lucchese, G. Raseev, and V. McKoy, Phys. Rev. A **25**, 2572 (1982).
[8] D. A. Rodham and G. A. Blake, Chem. Phys. Lett. **264**, 522 (1997).
[9] E. D. Glendening, J. Am. Chem. Soc. **118**, 2473 (1996); E. D. Glendening and D. Feller, J. Phys. Chem. **99**, 3060 (1995).
[10] W. Rudolph, M. H. Brooker, and C. C. Pye, J. Phys. Chem. **99**, 3793 (1995); C. C. Pye, W. Rudolph, and R. A. Poirier, *ibid.* **100**, 601 (1996).
[11] J. C. Polanyi and J. Wang, J. Phys. Chem. **99**, 13691 (1995); L. Manceron, A. Loutellier, and J. P. Perchard, Chem. Phys. **92**, 75 (1985); J. E. Combariza and N. R. Kestner, J. Phys. Chem. **99**, 2717 (1995).
[12] C. P. Schulz, R. Haugstätter, H. U. Tittes, and I. V. Hertel, Phys. Rev. Lett. **57**, 1703 (1986).
[13] C. Nitsch, C. P. Schulz, A. Gerber, W. Zimmermann-Edling, and I. V. Hertel, Z. Phys. D **22**, 651 (1992).
[14] M.-T. Lee, K. Wang, V. McKoy, and L. E. Machado, J. Chem. Phys. **97**, 3905 (1992).
[15] P. G. Burke, N. Chandra, and F. A. Gianturco, J. Phys. B **5**, 2212 (1972).
[16] A. R. Edmonds, *Angular Momentum in Quantum Mechanics* (Princeton University Press, Princeton, NJ, 1974).
[17] K. Wang and V. McKoy, J. Chem. Phys. **95**, 4977 (1991); S. N. Dixit and V. McKoy, Chem. Phys. Lett. **128**, 49 (1986); J. Xie and R. N. Zare, J. Chem. Phys. **93**, 3033 (1990).
[18] R. S. Mulliken, Phys. Rev. **59**, 873 (1941).
[19] K. Hashimoto and K. Morokuma, J. Am. Chem. Soc. **116**, 11436 (1994).
[20] S. Huzinaga and C. Arnau, J. Chem. Phys. **53**, 348 (1970).
[21] T. H. Dunning, Jr., J. Chem. Phys. **55**, 716 (1971).
[22] J. W. Cooper, Phys. Rev. **128**, 681 (1962).
[23] R. T. Wiedmann, R. G. Tonkyn, E. R. Grant, and M. G. White, J. Chem. Phys. **95**, 746 (1991).
[24] C. W. Bauschlicher, Jr., S. R. Langhoff, H. Partridge, J. E. Rice, and A. Komornicki, J. Chem. Phys. **95**, 5142 (1991).
[25] C. Nitsch, C. Hüglin, I. V. Hertel, and C. P. Schulz, J. Chem. Phys. **101**, 6559 (1994).
[26] D. Rodham, Ph.D. thesis, California Institute of Technology, 1997.

Downloaded 08 Mar 2006 to 131.215.225.174. Redistribution subject to AIP license or copyright, see http://jcp.aip.org/jcp/copyright.jsp